



Combining oxygen delivery and generation for targeted atherosclerosis therapy

Yujie Wang^{a,1}, Qianru Zhou^{b,1}, Le Lu^c, Jianhua Xu^d, Gang Yang^a, Xuan Sun^f, Xue Bao^f,
Lina Kang^f, Pin Lv^e, Renyuan Liu^e, Biao Xu^{f,***}, Qi Yang^{g,h,**},
Dan Mu^{a,b,d,e,*}, Bing Zhang^e

^a Department of Radiology, Nanjing Drum Tower Hospital Clinical College of Jiangsu University, No. 321 Zhongshan Road, Nanjing 210008, China

^b Department of Radiology, Nanjing Drum Tower Hospital Clinical College of Nanjing University of Chinese Medicine, No. 321 Zhongshan Road, Nanjing 210008, China

^c Department of Transfusion Medicine, Nanjing Drum Tower Hospital, The Affiliated Hospital of Nanjing University Medical School, No. 321 Zhongshan Road, Nanjing 210008, China

^d Yizheng Hospital of Nanjing Drum Tower Hospital Group, 1 Huannan Road, Living Area of Sinopec Yizheng Chemical Fibre CO., LTD., Yizheng 211900, Jiangsu, China

^e Department of Radiology, Nanjing Drum Tower Hospital, Affiliated Hospital of Medical School, Nanjing University, No. 321 Zhongshan Road, Nanjing 210008, China

^f Department of Cardiology, Nanjing Drum Tower Hospital, Affiliated Hospital of Medical School, Nanjing University, No. 321 Zhongshan Road, Nanjing 210008, China

^g Department of Radiology, Beijing Chaoyang Hospital, Capital Medical University, Beijing 100020, China

^h Key Lab of Medical Engineering for Cardiovascular Disease, Ministry of Education, Beijing 100020, China

ARTICLE INFO

Keywords:

Atherosclerosis
Oxygen delivery
Platelet membrane
Nanozymes

ABSTRACT

Hypoxia plays an important role in the progression of atherosclerosis. However, ameliorating hypoxia at atherosclerotic lesions remains a great challenge. To achieve targeted oxygen delivery to atherosclerotic plaques, Lipid 5-doped, platelet membrane-encapsulated magnetic mesoporous organosilicon nanoparticles loaded with perfluoro-15-crown ether (PFCE) (FMMON@PL) were prepared. PFCE worked as an oxygen carrier, while iron oxide nanoparticles (IONPs) acted as nanozymes with catalase-like activity to facilitate oxygen generation. To enhance plaque targeting, platelet membranes were coated onto mesoporous organosilicon nanoparticles containing PFCE and IONPs. Lipid 5 containing a tertiary amine was doped into the platelet membranes for lysosomal escape. Our results demonstrated that FMMON@PL specifically targeted macrophages in atherosclerotic plaques. FMMON@PL significantly reduced HIF-1 α expression, ameliorated oxidative stress, inhibited foam cell formation, and reduced M1 macrophage polarization. In conclusion, FMMON@PL successfully achieved oxygen delivery within plaques and inhibited plaque progression, demonstrating the feasibility of hypoxia alleviation for the treatment of atherosclerosis.

1. Introduction

Hypoxia accompanies the early onset and progression of atherosclerosis. Hypoxia may occur in areas of disturbed blood flow (e.g., aortic arch), which promotes endothelial injury and vascular dysfunction [1,2]. The increased permeability caused by endothelial injury leads to the lipid deposition into the subendothelium of the arteries [3,4]. Meanwhile, hypoxia also promotes reactive oxygen species (ROS)

generation and oxidative modification of low-density lipoprotein (ox-LDL) [5,6]. With the adhesion and infiltration of monocytes, macrophages are formed that phagocytose ox-LDL and transform into foam cells, which eventually form lipid core and promote plaque growth [7–9]. The high metabolic demand of macrophages and foam cells within the plaques directly contributes to plaque hypoxia, which in turn influences macrophage metabolic reprogramming and further promotes plaque development [10].

* Correspondence to: Dan Mu, Department of Radiology, Nanjing Drum Tower Hospital Clinical College of Jiangsu University, No. 321 Zhongshan Road, Nanjing 210008, China.

** Correspondence to: Qi Yang, Department of Radiology, Beijing Chaoyang Hospital, Capital Medical University, Beijing 100020, China.

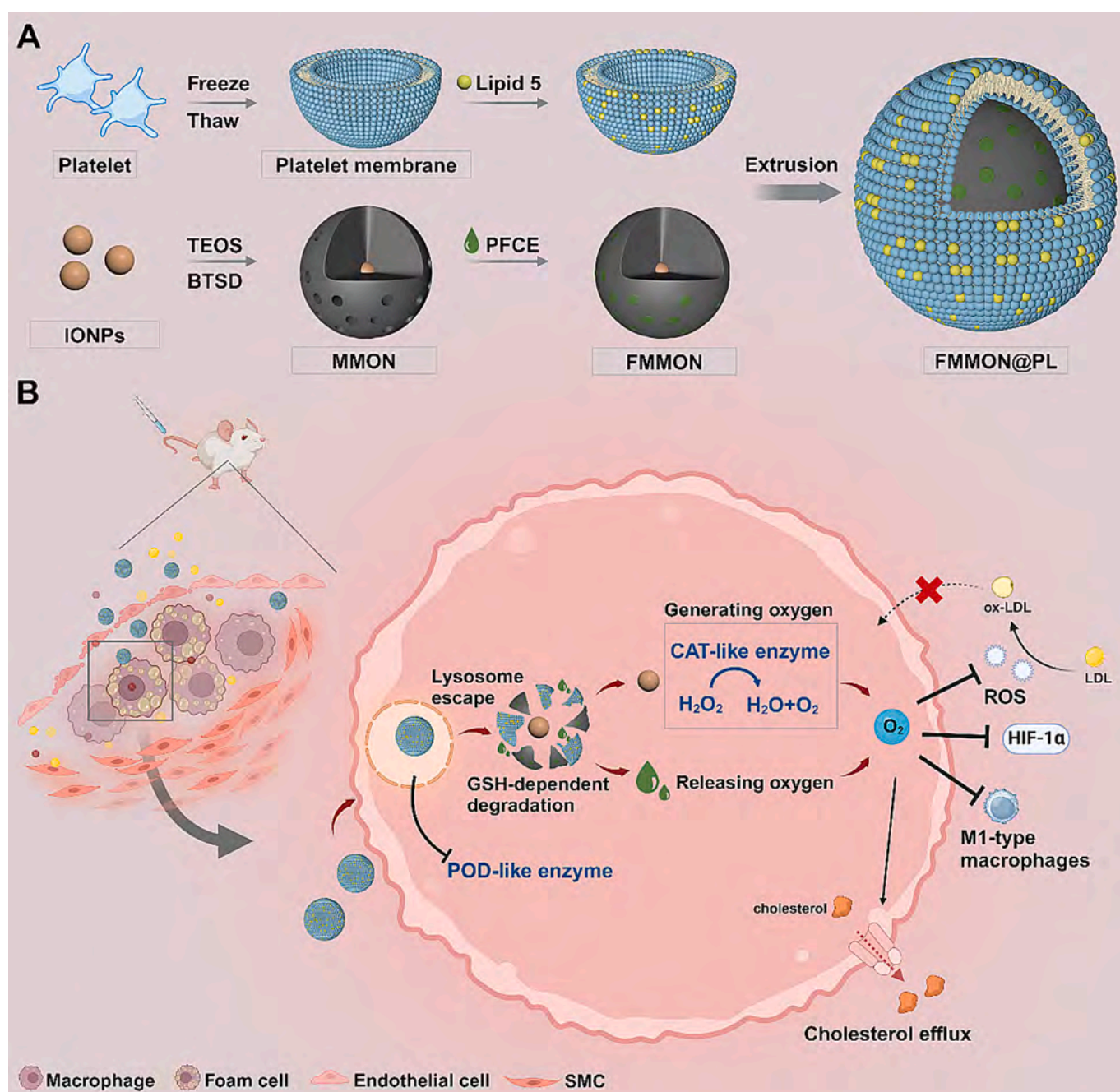
*** Correspondence to: Biao Xu, Department of Radiology, Beijing Chaoyang Hospital, Capital Medical University, 8 Gongren Tiyyuchang Nanlu, Beijing 100020, China.

E-mail addresses: xubiao62@nju.edu.cn (B. Xu), yangyangqiqi@gmail.com (Q. Yang), mudan118@126.com (D. Mu).

¹ These authors equally contributed to this work.

Hypoxia is involved in the progression of atherosclerosis mainly dependent on hypoxia-inducible factor-1 (HIF-1) [11]. HIF-1 is a key regulator of hypoxia that modulates the response of endothelial cells and macrophages to hypoxia [10–13]. HIF-1 is a heterodimeric protein consisting of HIF-1 β (whose activity is unaffected by hypoxia) and HIF-1 α (the reactive subunit) that is highly regulated by oxygen. Under non-hypoxic conditions, HIF-1 α can be degraded in an oxygen-dependent manner. During hypoxia, oxygen deficiency leads to HIF-1 α accumulation. In atherosclerotic plaques, elevated HIF-1 α leads to decreased cholesterol efflux from macrophages, promoting foam cell formation [14]. In addition, high expression of HIF-1 α promotes macrophage polarization to a pro-inflammatory M1 phenotype [15]. Thus, oxygen delivery-induced reduction of HIF-1 α expression has the potential to reduce lipid burden and improve the inflammatory microenvironment within atherosclerotic plaques.

Nanocarrier-dependent oxygen delivery is an effective approach to alleviate localized hypoxia, including oxygen carrying and oxygen generation strategies [16–18]. Oxygen carrying strategy utilizes oxygen carriers to achieve oxygen delivery. The effectiveness of perfluorocarbons (PFCs) as the most commonly used oxygen carriers has been extensively validated. PFC-based oxygen nanocarriers have been explored in a variety of diseases [19–21]. Oxygen generation strategy utilize the decomposition of some metal oxides to generate oxygen or the catalytic generation of oxygen from hydrogen peroxide using catalase (CAT) or CAT-like nanozymes [22–25]. For example, under neutral conditions, IONPs can efficiently catalyze the production of oxygen from hydrogen peroxide [25]. However, despite the fact that the hypoxic character of atherosclerosis is gradually recognized, the feasibility of alleviating hypoxia for the treatment of atherosclerosis remains unknown.



Scheme 1. Schematic illustration of (A) fabrication of FMMON@PL and (B) used for therapy of atherosclerosis.

In this study, we used a two-pronged strategy combining oxygen carrying and oxygen generation strategies. As the earliest discovered nanoenzymes, IONPs not only catalyze the production of oxygen from hydrogen peroxide, but are also widely used as MRI contrast agents in atherosclerosis [26–28]. However, the enzyme-like activity of IONPs is regulated by environmental pH values. In acidic environments, IONPs exhibit peroxidase (POD)-like enzyme activity (generating harmful hydroxyl radicals) [29–31], while CAT-like enzyme activity is exhibited in neutral environments [25]. To shield the unfavorable POD-like enzyme activity, IONPs were encapsulated inside degradable mesoporous organosilicon nanoparticles (MON) to generate magnetic MON (MMON). As oxygen carriers, perfluoro-crown ether (PFCE) was loaded into the mesopores of MMON to produce FMMON, which would further shield enzyme-like activities of IONPs. Finally, to improve the plaque targeting and lysosomal escape ability, Lipid 5 (phospholipid analogs with tertiary amines) was doped into platelet membranes [32], and then coated on the FMMON to generate FMMON@PL (Scheme 1A). After plaque-targeted FMMON@PL entered the plaque, oxygen gradually released from PFCE. Subsequently, FMMON@PL were taken up by macrophages/foam cells and trapped in lysosomes. In the acidic environment of the lysosomes, FMMON@PL remained structurally unchanged, thus effectively shielding POD-like enzyme activity of IONPs. With the assistance of Lipid 5, lysosomal escape was achieved and FMMON@PL entered the neutral cytoplasm. Glutathione (GSH) with high concentration in the cytoplasm degraded FMMON@PL, releasing the shielded IONPs. Eventually, CAT-like enzyme activity of IONPs was exhibited to produce oxygen *in situ* (Scheme 1B). The two-pronged strategy based on FMMON@PL directly ameliorated plaque hypoxia, leading to reduced ROS levels and HIF-1 α expression. Furthermore, FMMON@PL enhanced cholesterol efflux and inhibited uptake of ox-LDL, leading to reduced foam cell formation. Not only that, FMMON@PL also inhibited macrophage differentiation to proinflammatory M1-type macrophages, improving the proinflammatory environment within the plaque.

2. Materials and methods

2.1. Materials

IONPs (oleic acid-coated Fe₃O₄ nanoparticles) were provided by Nanjing XFNANO Materials Tech Co., Ltd. (Jiangsu, China). Hexadecyl trimethyl ammonium bromide (CTAB), tetraethyl orthosilicate (TEOS), tris(4, 7-diphenyl-1, 10-phenanthroline)ruthenium(II) dichloride complex ([Ru(dpp)₃]Cl₂) and rhodamine B (RhB) were purchased from Aladdin Reagent Co., Ltd. (Shanghai, China). Bis(triethoxysilylpropyl) disulfide (BTSD), fluorescein isothiocyanate (FITC), glutathione (GSH) were brought from Shanghai Yuanye Bio-Technology Co., Ltd. 1-Octylnonyl 8-[(2-hydroxyethyl)-8-(nonyloxy)-8-oxooctyl]amino]octanoate (Lipid 5), lipopolysaccharide (LPS), 2', 7'-dichlorodihydrofluorescein diacetate (DCF-DA) and (3-aminopropyl)triethoxysilane (APTES) were supplied by Shanghai Macklin Biochemical Co., Ltd. Cell Counting Kit-8 (CCK-8), 1, 1'-dioctadecyl-3, 3', 3'-tetramethylindocarbocyanine perchlorate (DiI), Lyso-Tracker Red, Amplex Red and Hoechst 33342 were purchased from Beyotime Biotechnology (Shanghai, China). Oxidized low-density lipoprotein (ox-LDL) and DiI-labeled ox-LDL (DiI-ox-LDL) were brought from Shanghai AngYu Biotechnology Co., Ltd. Primary antibodies, including anti-HIF-1 α , anti-CD68, anti-CD86, anti-CD206, were purchased from Abcam (China).

2.2. HIF-1 α expression

5×10^4 RAW264.7 cells were seeded in glass bottom dishes, and cultured in normoxia or hypoxia (1 % O₂, 5 % CO₂ and 94 % N₂) for 24 h. MON@PL, MMON@PL, FMON@PL and FMMON@PL (containing 50 μ g/mL of MON) were added and cultured for another 4 h. To observe intracellular localization, cells were stained with rabbit anti-HIF-1 α antibody overnight at 4 °C and then incubated with Alexa Fluor 647-

labeled goat anti-rabbit IgG secondary antibody for 1 h at room temperature. The nuclei were stained with the Hoechst 33342. Localization of HIF-1 α was observed by CLSM.

For quantitative analysis of HIF-1 α expression, 3×10^5 RAW264.7 cells were seeded in 6-well plates and incubated in normoxia (95 % air and 5 % CO₂) or hypoxia (1 % O₂, 5 % CO₂ and 94 % N₂) for 24 h. MON@PL, MMON@PL, FMON@PL and FMMON@PL (containing 50 μ g/mL of MON) were added and cultured for another 4 h. After washed with PBS for three times, cells were collected and HIF-1 α expression was determined by quantitative polymerase chain reaction (qPCR) and Western Blot.

2.3. Uptake of ox-LDL

RAW264.7 were seeded in 12-well or 96-well plates and glass bottom dishes and cultured overnight. After starvation for 24 h, cells were incubated in hypoxia (1 % O₂, 5 % CO₂ and 94 % N₂) for another 6 h. Then, cells were incubated with MMON@PL, FMON@PL or FMMON@PL (containing 50 μ g/mL of MON) for 12 h. The medium was replaced with fresh medium containing ox-LDL or DiI-ox-LDL (50 μ g/mL). After incubation for 24 h, cells were washed with cold PBS. After stained with Oil Red O (ORO) for optical visualization and quantitative analysis for absorbance at 492 nm using a microplate reader. Or, cells were stained with Hoechst 33342 for visualization by CLSM or quantitatively analyzed by flow cytometry.

2.4. Macrophages polarization

To study the macrophage polarization *in vitro*, RAW264.7 were seeded in 6-well plates and cultured overnight. The medium was replaced with N₂-saturated fresh medium, cultured in hypoxia (1 % O₂, 5 % CO₂ and 94 % N₂) for 5 min and placed in normoxia for 10 min. The hypoxia-normoxia cycle was repeated for 12 times to induce M1-type macrophages [33,34]. At last, MMON@PL, FMON@PL and FMMON@PL (containing 50 μ g/mL of MON) were added and incubated with cells for 24 h. The medium was collected to measure IL-6 and TNF- α by mouse IL-6 and TNF- α ELISA Kits (Beyotime). Cells were washed by cold PBS. PE-labeled CD86 antibody (Abcam) and APC-conjugated CD206 antibody (Abcam) were added and incubated at 4 °C for 1 h, respectively. Cells were collected and analyzed by flow cytometry. Or, cells were stained with Hoechst 33342 and observed by CLSM.

2.5. Treatment protocol

ApoE^{-/-} mice were fed with a high-fat diet. After 4 weeks, mice were randomized into four groups ($n = 6$). The mice were intravenously injected with saline (control), MMON@PL, FMON@PL and FMMON@PL at a dose of 2 mg/kg iron via tail vein weekly for 4 weeks. The body weight of the mice was recorded before each administration. After 2 weeks, mice were sacrificed to collect aortas, blood and major organs to evaluate therapeutic effect.

2.6. Histological analysis

Aortas were fixed by perfusion of 4 % paraformaldehyde. After the removal of the periaortic tissues, aortas were dissected longitudinally and stained with Oil Red O (ORO). Histological analysis was performed by hematoxylin-eosin (H&E) staining and Masson's trichrome staining.

For immunohistochemistry analysis, frozen sections of aortas were permeabilized and blocked using a solution containing 0.1 % Triton X-100 in 5 % BSA. Then, the sections were incubated with the primary antibodies at 4 °C overnight. After washed with PBST for five times, the sections were incubated with appropriate secondary antibodies at room temperature for 1 h. After washed with PBST, the sections were stained with DAPI for fluorescent visualization.

2.7. Statistical analysis

Results are presented as the mean \pm standard deviation (SD). Statistical comparisons were made by unpaired Student's *t*-test (between two groups). Data analysis and figures were prepared using the Graph-Pad Prism software (Version 7.0).

3. Results and discussion

3.1. Preparation and characterization of FMMON@PL

MMON containing IONPs were first synthesized with an average diameter of 55.3 nm (Fig. 1A). MMON exhibited spherical morphology with at least one magnetic particle located at MMON's center (Fig. 1B). The average amount of iron in MMON was measured to be 16.7 $\mu\text{g}/\text{mg}$, and the encapsulation efficiency of iron was calculated to be 33.4 %. In addition, the mesopores of MMON can be clearly observed, which provided space for PFCE filling. As proved by TEM-EDS mapping (Fig. 1C)

and ^{19}F NMR (Fig. S1), PFCE was successfully loaded into MMON to generate FMMON. The amount of PFCE in FMMON was calculated to be 0.64 $\mu\text{mol}/\text{mg}$. And thus, the encapsulation efficiency of PFCE was 2.2 %. Importantly, fluorine can be observed throughout MMON in the images of TEM-EDS mapping, suggesting complete shielding of IONPs. In order to improve the capability of targeting atherosclerotic plaques, platelet membranes were coated onto the surface of FMMON to generate FMMON@P. And Lipid 5 was doped into platelet membranes to equip the nanoparticles with lysosomal escape. The amount of doped Lipid 5 was determined by Zeta potential of MMON@P. It gradually increased with the increase of mass ratio of Lipid 5/MMON (Fig. S2). However, over-doped Lipid 5 may lead to premature clearance *in vivo* [32]. Ultimately, the mass ratio of Lipid 5/MMON was determined to be 2:1 to produce FMMON@PL. As shown in Fig. 1D, the average diameter of FMMON@PL was 79.6 nm, larger than that of MMON. It was explained by that coating of platelet membranes increased the hydrated particle size. Similar to MMON, FMMON@PL showed uniform morphology and spherical structures as shown in Fig. 1E and F. In addition, the

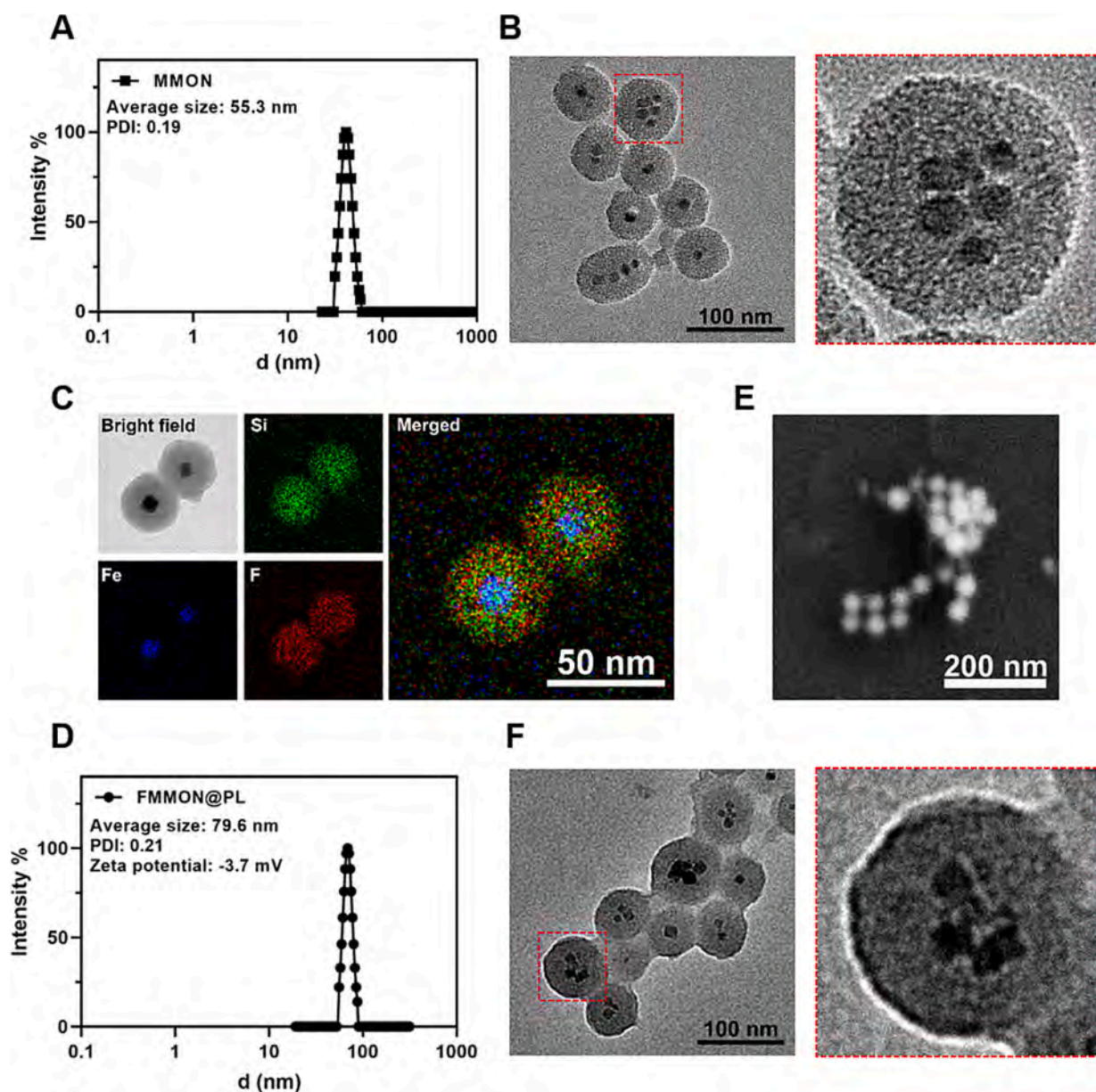


Fig. 1. (A) Size distribution and (B) morphology of MMON. (C) Energy dispersive X-ray spectroscopy (EDS) elemental mapping of FMMON. (D) Size distribution of FMMON@PL. (E) SEM and (F) TEM images of FMMON@PL.

mesopores of MMON can hardly be observed, indicating PFCE filling and coating of platelet membranes (Fig. 1F). Western blot analysis also verified that characteristic platelet membrane proteins, including CD42b, CD47 and CD42b, were present on FMMON@PL, indicating successful translocation of platelet membrane to FMMON (Fig. S3).

3.2. Oxygen carrying and oxygen generation

To verify oxygen release from PFCE, oxygen release was detected from oxygen-saturated saline, MMON, FMMON and FMMON@PL. As shown in Fig. 2A, all groups exhibited similar oxygen release within 1 h, which was attributed to the rapid release of dissolved oxygen from the water. Oxygen release in MMON was comparable to saline, while

FMMON exhibited enhanced oxygen release. Specifically, oxygen release in FMMON was 2.3 times higher than in MMON within 2 h. Interestingly, the oxygen release of FMMON@PL was only 52.5 % of that of FMMON within 2 h. In addition, FMMON almost released all oxygen within 3 h, whereas oxygen release from FMMON@PL lasted for 6 h. FMMON@PL exhibited a sustainable oxygen release compared with FMMON, given a similar total amount of oxygen. This may be attributed to the slow release of oxygen due to platelet membrane coating. In addition, O₂ release efficiency from PFCE can be calculated to be 66.2 %.

In the transmembrane transport of oxygen, oxygen is transported along the cell membrane or organelle membrane rather than in water due to the higher solubility of oxygen in the phospholipid bilayer compared to water [35]. Thus, the released oxygen from FMMON@PL

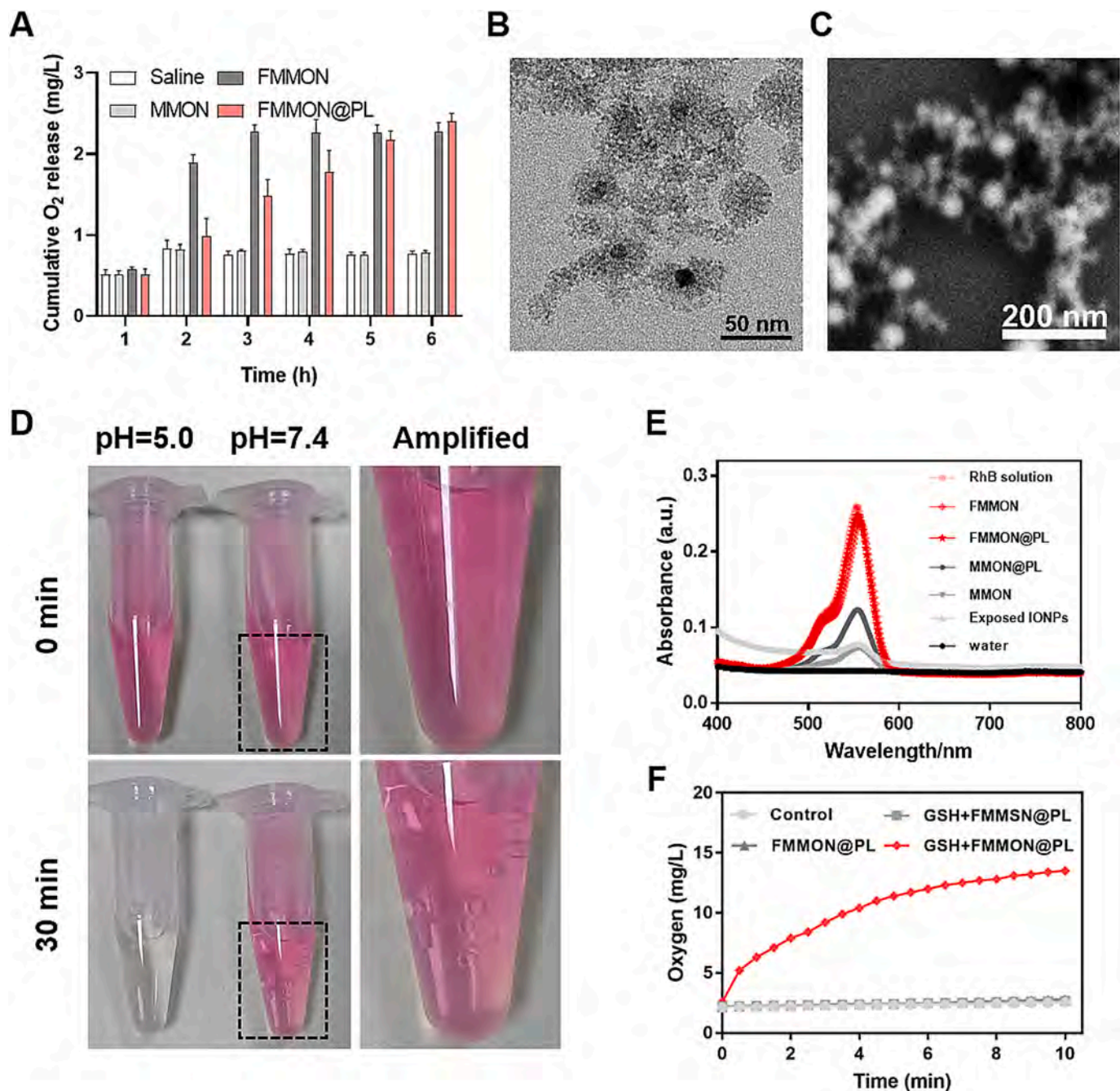


Fig. 2. (A) Oxygen release from MMON, FMMON and FMMON@PL. (B) TEM and (C) SEM images of MMON after treatment with 10 mM of GSH for 6 h. (D) Images of enzyme-like activities of FMMON@PL pretreated with GSH at pH 5.0 and pH 7.4. (E) Absorption spectra of RhB treated with IONPs, MMON, FMMON, MMON@PL and FMMON@PL at pH 5.0. (F) Oxygen generation in H₂O₂ solution at pH 7.4 with different formulations.

first accumulated in the platelet membrane, forming an oxygen shield that slowed down the further release of oxygen. In addition, unlike FMMON, the hydrophilic layer of platelet membrane on the surface of FMMON@PL may form the “unstirred water layer” [35], which prevent the exchange of substances between the platelet membrane and water, further reducing the rate of oxygen release.

The slow release of oxygen facilitates FMMON@PL plaque-targeted oxygen delivery *in vivo*. In response to the low-oxygen environment of the veins, FMMON may have released all oxygen before they reach the plaque, whereas the platelet membrane may ensure efficient plaque oxygen delivery via targeting the plaque and slowing oxygen release.

To initiate oxygen generation, FMMON@PL must degrade to expose

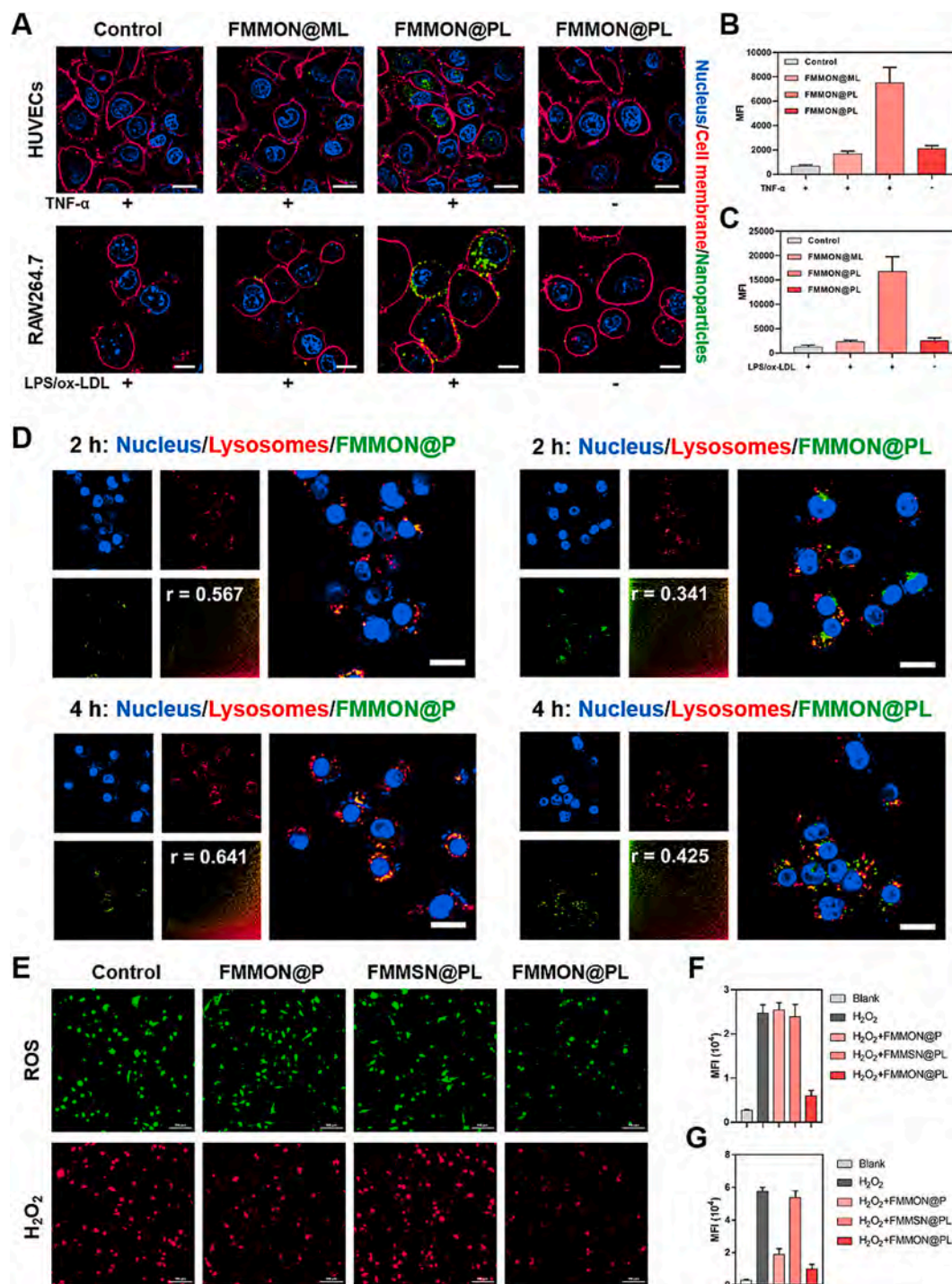


Fig. 3. (A) Confocal images of TNF- α -activated HUVECs and LPS/ox-LDL-activated RAW264.7 incubated with FMMON@ML and FMMON@PL. Nucleus was stained with Hoechst 33342 (blue), cell membranes were stained with DiI (red) and nanoparticles (FMMON@ML and FMMON@PL) were labeled with FITC (green). Scale bar: 10 μ m. Quantitative analysis of (B) activated HUVECs and (C) activated RAW264.7 incubated with FMMON@ML and FMMON@PL. (D) Confocal images of activated RAW264.7 incubated with FMMON@P or FMMON@PL (green) for 2 h and 4 h. Lysosomes were labeled with Lysotracker Red. Scale bar: 20 μ m. (E) Confocal imaging of ROS and levels in H₂O₂-pretreated RAW264.7 treated different nanoparticles. Quantitative analysis of intracellular (F) ROS and (G) H₂O₂ levels in H₂O₂-pretreated RAW264.7 incubated with different groups. (For interpretation of the references to colour in this figure legend, the reader is referred to the web version of this article.)

IONPs. As shown in Fig. 2B and C, FMMON@PL lost the spherical shape after incubation with 10 mM GSH for 6 h, accompanied by some irregular clumps. Most importantly, exposed IONPs could be clearly observed (Fig. 2B). As a comparison, MMSN (containing no disulfide bonds) were not vulnerable to GSH and still remained structurally intact (Fig. S4), indicating GSH-dependent degradation of MMON.

As described before, enzyme-like activities of IONPs depend on pH values of environment. As shown in Fig. 2D, after degradation of FMMON@PL, exposed IONPs exhibited POD-like activity at pH 5.0 to generate $\cdot\text{OH}$, inducing degradation and discoloration of RhB [36], while exhibiting CAT-like activity at pH 7.4 to generate oxygen. POD-like enzyme activity was successfully inhibited by burying IONPs in the core of MMON and sealing with PFCE. As shown in Fig. 2E, 83.5 % of RhB was degraded by exposed IONPs in the presence of H_2O_2 at pH 5.0, and it was 62.8 % by MMON@PL. However, only 5.1 % of RhB was degraded by FMMON@PL in the same conditions. These results also suggested that the sealing of PFCE played a major role in inhibiting the activity of POD-like enzyme activity. As shown in Fig. 2F, degassed FMMON@PL did not catalyze the production of oxygen in the presence of H_2O_2 at pH 7.4. However, obvious oxygen generation was detected after FMMON@PL were pretreated with GSH. Oxygen generation efficiency of degraded FMMON@PL was revealed by H_2O_2 consumption. As shown in Fig. S5, 37.5 % of H_2O_2 was consumed by degraded FMMON@PL within 3 h. However, in the same condition, FMMSN@PL with pretreated with GSH barely catalyzed the production of oxygen. Overall, the dual enzyme-like activities of FMMON@PL were no longer entirely dependent on pH of the environment, but rather on their structural integrity.

3.3. Cellular uptake and lysosomal escape

Platelet-membrane coated nanoparticles are capable of specifically binding impaired vascular endothelial cells and macrophage-derived foam cells. In this study, cellular uptake of FMMON@PL was evaluated against TNF- α -activated HUVECs and LPS/ox-LDL-activated RAW264.7 cells. As shown in Fig. 3A, compared with FMMON@ML (containing no platelet membranes), FMMON@PL can obviously bind to and be internalized into activated HUVECs and activated RAW264.7 cells. In addition, FMMON@PL were barely internalized into non-activated HUVECs and RAW264.7 cells, which facilitated specific targeting. These results were supported by quantitative results of flow cytometry. Specifically, mean fluorescence intensity (MFI) of FMMON@PL in activated HUVECs was 4.5 times higher than that of FMMON@ML (Fig. 3B and S6). And that was 7.3 times higher than that of FMMON@ML in activated RAW264.7 cells (Fig. 3C and S7). These results demonstrated more efficient targeting of FMMON@PL to damaged endothelial cells and foam cells compared to FMMON@ML.

Endothelial damage is the initial stage of plaque formation and is prevalent in plaque progression. However, as the plaque progresses, foam cells gradually form and dominate plaque vulnerability. Interestingly, it appeared that activated RAW264.7 cells took up more FMMON@PL compared to activated HUVECs. Under the same conditions, activated RAW264.7 cells internalized 3.1 times more FMMON@PL than activated HUVECs detected by flow cytometry and 5.5 times measured by a microplate reader (Fig. S8). These results suggested that FMMON@PL exhibited higher affinity for foam cells.

After being internalized into cells, the ability to lysosomal escape determined the enzyme-like effect of FMMON@PL and cell fate. As shown in Fig. 3D, FMMON@P (containing no Lipid 5) co-localized with lysosomes (yellow area), while FMMON@PL showed significant lysosomal escape (green area) after incubation with cells for 2 h or 4 h. Pearson correlation coefficients (r) were calculated and used to measure the ratio of co-localization of FMMON@PL with lysosomes. $r > 0.5$ indicates co-localization, while $r < 0.5$ indicates no co-localization. Specifically, r of FMMON@P was 0.567 and 0.641, respectively, while r of FMMON@PL was 0.341 and 0.425, respectively, after incubated for 2 h

and 4 h.

3.4. Reducing ROS

After lysosomal escape, FMMON@PL can reduce ROS levels by consuming H_2O_2 . As shown in Fig. 3E, levels of ROS and H_2O_2 were revealing by ROS and H_2O_2 probes, respectively. FMMON@P hardly lowered ROS levels, but did reduce H_2O_2 . It was explained by that FMMON@P were trapped in lysosomes and exhibited POD-like activity after degradation. FMMSN@PL had little effect on the levels of ROS and H_2O_2 due to the fact that FMMSN@PL cannot be degraded by GSH. FMMON@PL can significantly reduce ROS levels by consuming H_2O_2 . Specifically, ROS were reduced by more than 75 % (Fig. 3F and S9) compared to the other groups, accompanied by consuming 82.7 % of H_2O_2 (Fig. 3G and S10). In contrast, FMMON@P consumed 67.4 % of H_2O_2 , but ROS were instead elevated by 6.0 %, which led to severe cytotoxicity of FMMON@P. Cell viability of FMMON@P was 43 % against H_2O_2 -pretreated RAW264.7 (Fig. S11) and 60 % against LPS/ox-LDL-activated RAW264.7 (Fig. S12), while that of FMMON@PL was 96 % and 99 %, respectively. The massive death of foam cells may promote the formation of necrotic cores in plaques and favor plaque vulnerability. Therefore, timely lysosomal escape is beneficial not only for reducing ROS but also for avoiding cell death.

3.5. Alleviating hypoxia and reducing HIF-1 α expression

To clarify the role of PFCE and IONPs, MON@PL (containing no PFCE and IONPs) were first tested. Changes in intracellular oxygen were monitored using a hypoxia probe ($[\text{Ru}(\text{ddp})_3]\text{Cl}_2$) whose fluorescence signals can be dynamically quenched by molecular oxygen. As shown in Fig. S13A and S13B, the fluorescence signals (red) of $[\text{Ru}(\text{ddp})_3]\text{Cl}_2$ in RAW264.7 under hypoxic conditions were extremely elevated compared with that under normoxic conditions. MON@PL hardly quenched the fluorescence signals, suggesting no capability to ameliorate hypoxia. This is because MON@PL can neither carry oxygen nor produce oxygen. Therefore, as shown in Fig. S13C, S13D and S13E, MON@PL also failed to reduce HIF-1 α expression.

As shown in Fig. 4A, MMON@PL (containing no PFCE) and FMON@PL (containing no IONPs) added can significantly quench the fluorescence signals, indicating the effectiveness of oxygen carrying and oxygen production. Notably, FMMON@PL exhibited the most quenching of $[\text{Ru}(\text{ddp})_3]\text{Cl}_2$ fluorescence, indicating the most oxygen delivery by combination of oxygen carrying and generation. The addition of MMON@PL and FMON@PL quenched 35.8 % and 46.7 % of the fluorescence, respectively, while FMMON@PL quenched 73.3 % compared to hypoxia (Fig. 4B).

In normoxia, HIF-1 α is rapidly degraded by the ubiquitin-proteasome, whereas degradation of HIF-1 α subunit is inhibited in hypoxia. The undegraded HIF-1 α and HIF-1 β form active HIF-1, which is transported to the nucleus to regulate the transcription of a variety of genes. As shown in Fig. 4C, HIF-1 α was overexpressed and dominantly translocated into the cell nuclei in hypoxia compared with that in normoxia. MMON@PL, FMON@PL and FMMON@PL can inhibit expression and of HIF-1 α . At protein level, the inhibitory effect of FMMON@PL on HIF-1 α was comparable to FMON@PL and higher than that of MMON@PL. Expression of HIF-1 α was reduced by 51.2 % by MMON@PL, 62.1 % by FMON@PL and 63.4 % by FMMON@PL as shown in Fig. 4D. Interestingly, at mRNA level, the inhibitory effect of FMMON@PL on HIF-1 α was higher than that of both MMON@PL and FMON@PL. Expression of HIF-1 α mRNA was reduced by 58.5 % by MMON@PL, 56.8 % by FMON@PL and 71.9 % by FMMON@PL (Fig. 4E). However, FMMON@PL inhibited nuclear translocation of HIF-1 α significantly better than MMON@PL and FMON@PL as shown in the magnified view of Fig. 4C.

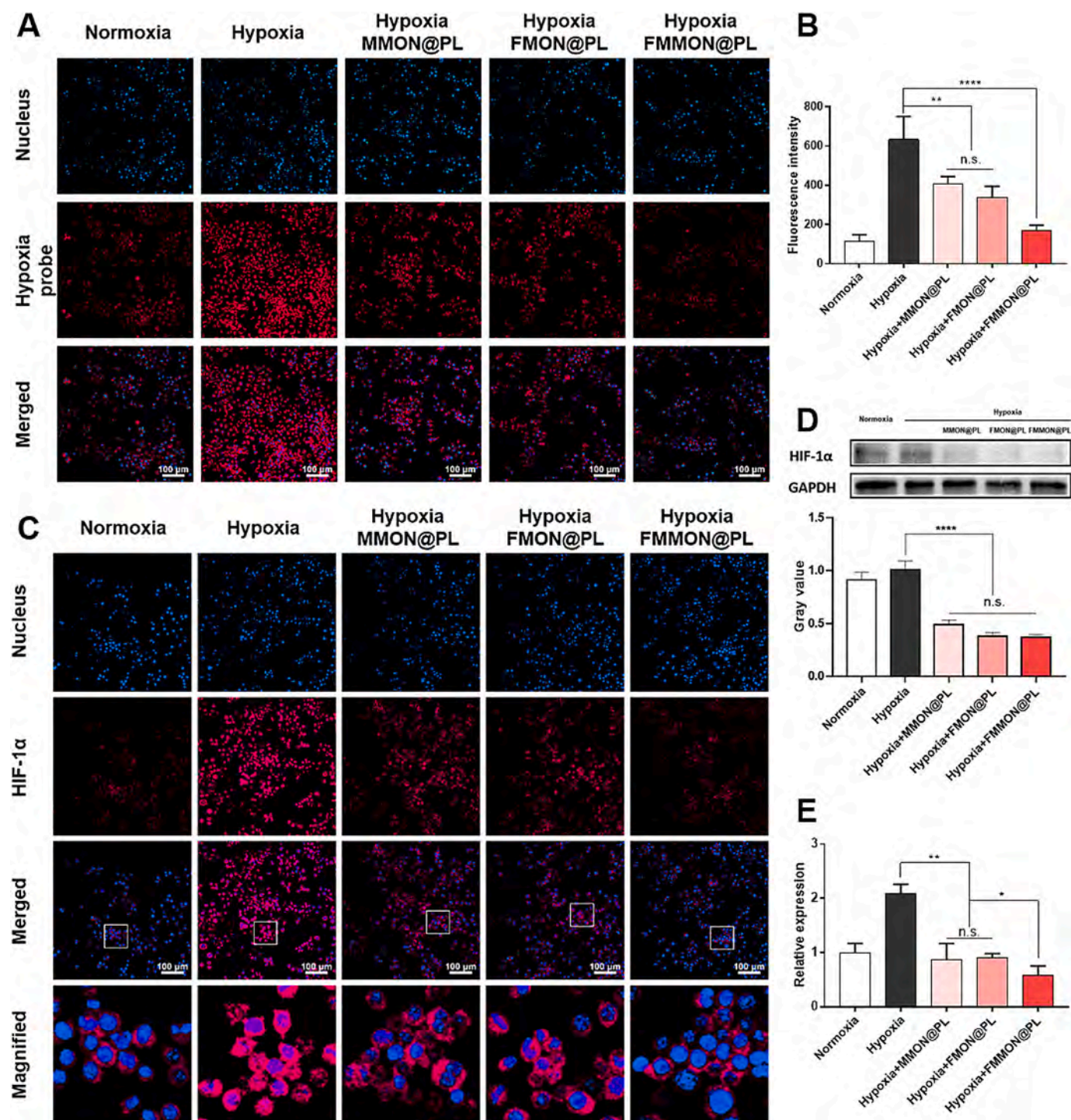


Fig. 4. (A) Confocal images and (B) quantitative analysis of RAW264.7 in hypoxia after treatment with MMON@PL, FMON@PL and FMMON@PL. (C) CLSM observation of HIF-1α expression and its nuclear translocation in RAW264.7. (D) Western blot of HIF-1α expression in RAW264.7 in hypoxia after various treatments. (E) mRNA levels of HIF-1α in RAW264.7 in hypoxia after various treatments. * $P < 0.05$, ** $P < 0.01$ and **** $P < 0.0001$. n.s., not significant.

3.6. Inhibition of foam cell formation

Studies have shown that inhibition of HIF-1α downregulates genes associated with fat storage, fatty acid elongation, and cholesterol metabolism, suggesting that oxygen delivery has the potential to reduce lipid burden and inhibit foam cell formation [14]. As shown in Fig. 5A, hypoxia induced accumulation of lipid droplets in macrophages, which is consistent with the previous report [37]. MMON@PL, FMON@PL and FMMON@PL significantly inhibited the accumulation of lipid droplets

in macrophages, and FMMON@PL exhibited the best inhibition effect. Specifically, cellular uptake of ox-LDL was inhibited by 38.7 % and 46.0 % by MMON@PL and FMON@PL respectively compared to control, while it was 77.4 % by FMMON@PL revealed by ORO staining. Results in Fig. 5B also suggested the best inhibition of ox-LDL uptake by FMMON@PL. Ox-LDL uptake was inhibited by 55.6 % and 61.2 % by MMON@PL and FMMON@PL respectively, while it was 89.4 % by FMON@PL revealed by the results of flow cytometry (Fig. 5C and S14).

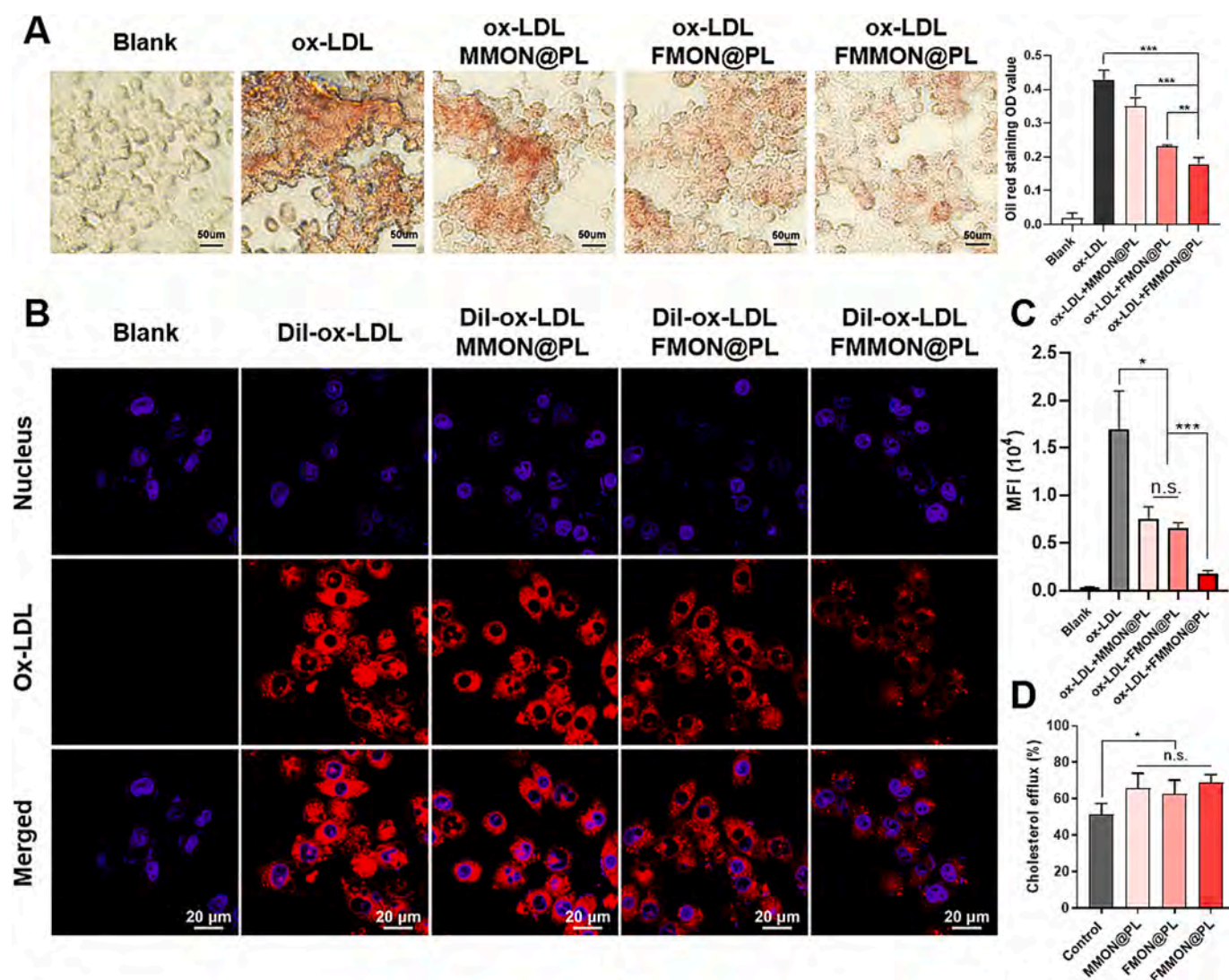


Fig. 5. (A) Representative images and quantification of Oil Red O (ORO) staining of RAW264.7 treated with MMON@PL, FMON@PL and FMMON@PL. (B) Cellular uptake and (C) quantitative analysis of DiI-ox-LDL in RAW264.7 treated with MMON@PL, FMON@PL and FMMON@PL. (D) Cholesterol efflux rate in RAW264.7 treated with MMON@PL, FMON@PL and FMMON@PL. * $P < 0.05$, ** $P < 0.01$, *** $P < 0.001$ and **** $P < 0.0001$. n.s., not significant. (For interpretation of the references to colour in this figure legend, the reader is referred to the web version of this article.)

To clarify the role of FMMON@PL, cholesterol efflux was performed and the results were shown in Fig. 5D. MMON@PL, FMON@PL and FMMON@PL showed improved cholesterol efflux. In specific, cholesterol efflux was increased by 27.7 %, 21.6 % and 33.2 % by MMON@PL, FMON@PL and FMMON@PL respectively compared to control group. These results suggested that oxygen delivery based on FMMON@PL can inhibit ox-LDL uptake and promote cholesterol efflux, thus suppressing foam cell formation.

3.7. Inhibition of M1-type macrophages

Within plaques, macrophages are polarized into the M1 phenotype and M2 phenotype. M1-type macrophages promote foam cell formation and inflammatory progression, ultimately leading to atherosclerotic lesion and plaque instability. In contrast, M2-type macrophages promote tissue remodeling, repair, and removal of dead cells and debris, which facilitates regression of atherosclerotic plaques [38]. However, hypoxia promotes macrophage polarization to a pro-inflammatory M1 phenotype, promoting foam cell formation and the inflammatory microenvironment. Interestingly, oxygen delivery based on FMMON@PL significantly inhibited macrophage polarization to a pro-inflammatory

M1 phenotype. As shown in Fig. 6A and B, hypoxia successfully induced polarization of macrophages to M1 phenotype, as evidenced by elevated expression of CD86 (M1 phenotype marker). MMON@PL, FMON@PL and FMMON@PL all significantly reduced CD86 expression. Among them, FMMON@PL showed the best inhibition of CD86 (M2 phenotype marker) expression. Specifically, CD86 expression was reduced by 68.8 %, 54.9 % and 78.6 %, respectively, by MMON@PL, FMON@PL and FMMON@PL (Fig. 6C). It should be noted that MMON@PL, FMON@PL and FMMON@PL did not increase CD206 expression, suggesting that oxygen did not modulate M1-to-M2 polarization.

Decreased M1-type macrophages reduced the expression of inflammatory factors. As shown in Fig. 6D, TNF- α expression was reduced by 52.4 %, 54.6 % and 73.2 % by MMON@PL, FMON@PL and FMMON@PL respectively. Similarly, IL-6 expression was also reduced by 36.0 % and 78.9 % by FMON@PL and FMMON@PL respectively. However, IL-6 expression was increased by 29.5 % by MMON@PL (Fig. 6E). This may be caused by POD-like enzyme activity of unshielded IONPs. These results suggested that FMMON@PL altered the inflammatory microenvironment of plaques, exhibiting great potential for improving plaque stability.

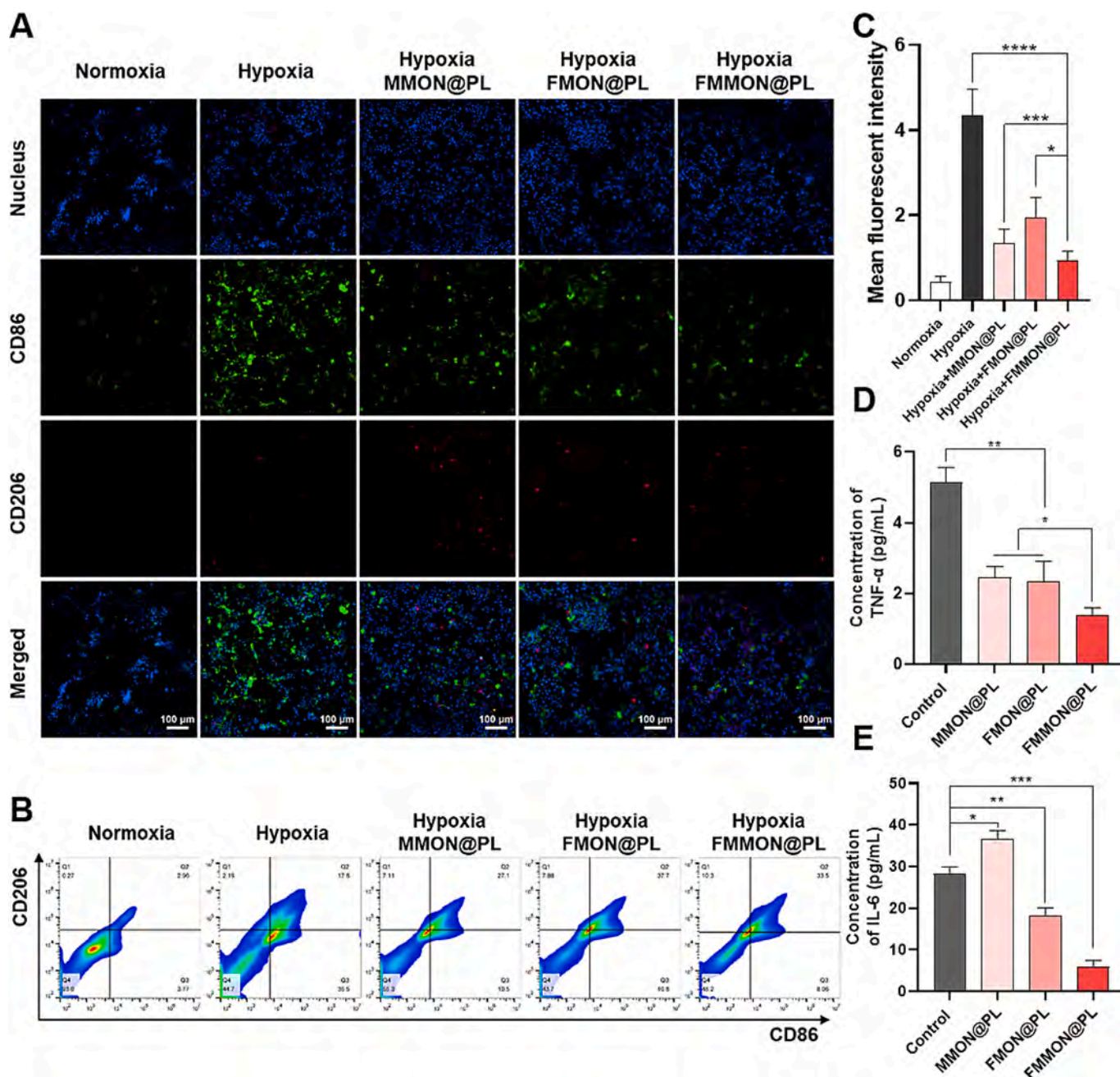


Fig. 6. (A) Immunofluorescence images of double staining for CD68 and CD206 to label M1 or M2 phenotype macrophages. (B) Flow cytometry analysis of the macrophage phenotypes after different treatment. (C) Mean fluorescent intensity of CD86 after different treatment. Expression of (D) TNF- α and (E) IL-6 after different treatment. * $P < 0.05$, ** $P < 0.01$, *** $P < 0.001$ and **** $P < 0.0001$.

FMMON@PL-based oxygen therapy for atherosclerosis involves combating oxidative stress, inhibiting foam cell formation and inhibiting the formation of M1-type macrophages thereby reducing the inflammatory response. One of the key regulators is HIF-1 α . Plaque growth directly contributes to the difficulty of diffusing oxygen deep into the artery walls. Oxygen consumption is also exacerbated by the high metabolic demands of macrophages and foam cells within the plaque. Both promote high expression of HIF-1 α within the plaque. First, HIF-1 α regulates the expression of various genes that affect oxidative stress and redox homeostasis. In atherosclerotic lesions, increased oxidative stress damages endothelial cells and promotes oxidation of lipids (LDL), which in turn triggers further inflammatory responses. Secondly, HIF-1 α further promotes monocyte and macrophage infiltration by upregulating the expression of pro-inflammatory cytokines

(TNF- α , etc.). Finally, HIF-1 α also promotes lipid accumulation in arterial endothelial cells and macrophages by regulating the expression of genes related to lipid metabolism, further promoting foam cell formation. To summarize, HIF-1 α drives the progression of atherosclerosis at different levels and increases the risk of cardiovascular events.

3.8. Plaque-targeting in vivo

Atherosclerotic plaques were constructed in the aorta of ApoE^{-/-} mice by feeding a high-fat diet. To verify the plaque-targeting behavior, FITC-labeled FMMON@ML and FMMON@PL were administrated intravenously. After 24 h, mice were sacrificed and aortas were collected and visualized by fluorescence imaging. As shown in Fig. 7A, large areas of FITC fluorescence were observed in aorta treated with FMMON@ML

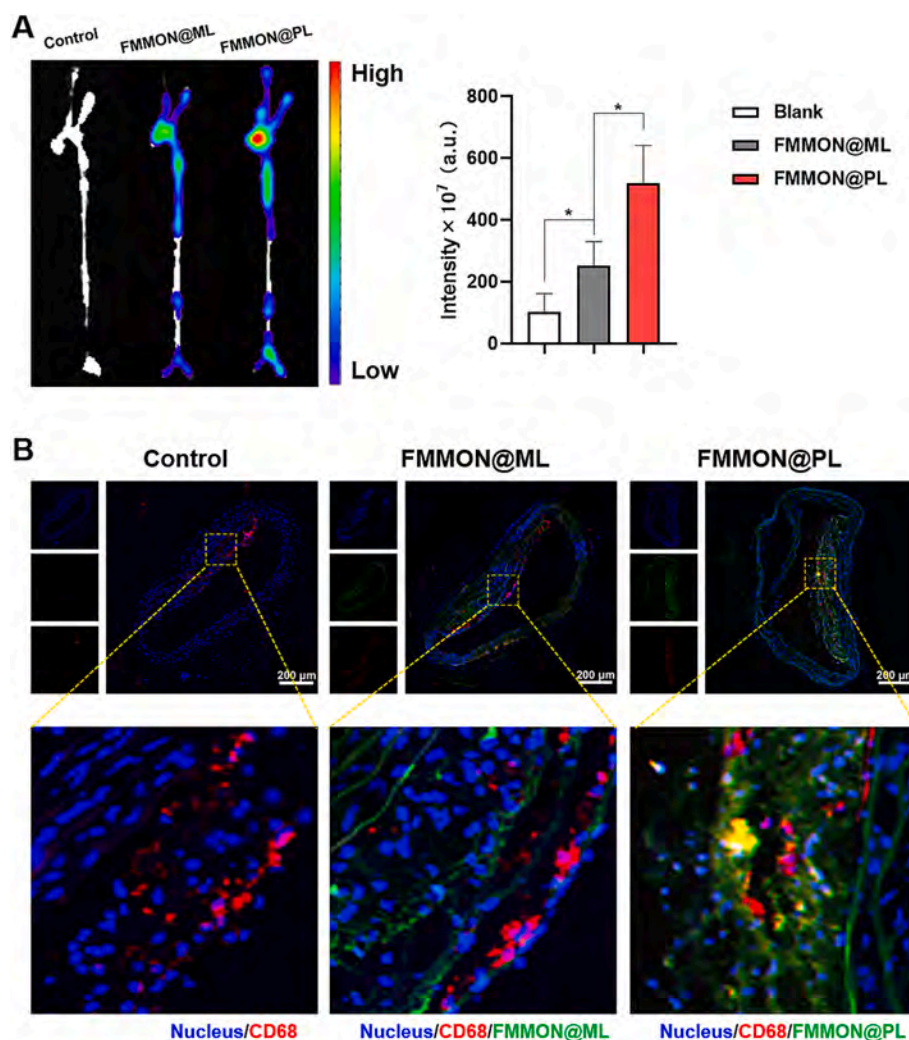


Fig. 7. (A) Representative *ex vivo* images and fluorescent intensity of aortas with plaques from ApoE^{-/-} mice treated with FITC-labeled FMMON@ML and FMMON@PL. (B) Deposition of FITC-labeled FMMON@ML and FMMON@PL in aortic plaques. Nucleus was stained with DAPI (blue), and macrophages were labeled via CD68 staining (red). **P* < 0.05. (For interpretation of the references to colour in this figure legend, the reader is referred to the web version of this article.)

and FMMON@PL, and the aortic arch, which is most prone to plaque formation, showed the strongest FITC fluorescence. More importantly, aorta treated with FMMON@PL exhibited stronger fluorescence than FMMON@ML, suggesting enhanced targeting of FMMON@PL to plaques. Specifically, the fluorescence intensity of the FMMON@PL group was 2.06 times higher than that of FMMON@ML. In addition, carotid arteries also showed significant FITC fluorescence, indicating plaque formation. T₂-MRI in carotid arteries also demonstrated plaque-targeting and accumulation of FMMON@PL (Fig. S15). In order to examine the distribution of FMMON@PL within the plaque, colocalization of macrophages (CD68) and FMMON@PL were performed as shown in Fig. 7B. As a comparison, FMMON@ML accumulated in the plaque barely co-localized with macrophages. However, obvious colocalization of FMMON@PL with macrophages can be clearly observed. These results suggested specific targeting of FMMON@PL to macrophages in atherosclerotic plaques.

3.9. Therapeutic effects and biosafety

To explore the anti-atherosclerosis effect of FMMON@PL, atherosclerotic ApoE^{-/-} mice were randomly grouped into four groups followed by the treatment of saline (control), MMON@PL, FMON@PL and FMMON@PL via tail veins once a week for 4 weeks (Fig. 8A). Throughout the treatment, MMON@PL, FMON@PL and FMMON@PL

did not cause significant changes in the body weight of the mice (Fig. S16). MMON@PL, FMON@PL and FMMON@PL significantly reduced the lesion area, while FMMON@PL showed the best therapeutic effect. In specific, lesion area was reduced by 41.4 %, 48.8 % and 62.3 % by MMON@PL, FMON@PL and FMMON@PL respectively (Fig. S17). After therapy, plaque size was remarkably reduced as evidence by H&E (Fig. 8B) and Masson staining (Fig. S18). In addition, the expression of HIF-1α with plaques was consistently reduced (Fig. 8B). With the decreased expression of HIF-1α, oxidative stress within the plaque was also alleviated. The fluorescence of 4-HNE (an oxidative stress biomarker) was visualized by CLSM. As expected, the fluorescence of 4-HNE was dramatically weakened. These results suggested that that oxygen carrying and oxygen generation can effectively inhibit HIF-1α expression and oxidative stress, and the combination of the two strategies showed better inhibition effect.

After treatment, the level of inflammatory factors (TNF-α, IL-6) decreased. TNF-α expression was reduced by 50.0 %, 53.8 % and 65.9 % by MMON@PL, FMON@PL and FMMON@PL respectively. Similarly, IL-6 expression was also reduced by 27.1 % and 56.1 % by FMON@PL and FMMON@PL (Fig. S19), while it was increased by 57.8 % by MMON@PL, which was similar to the results in Fig. 6. The decrease of inflammatory factors was mainly due to the inhibition of formation of M1 macrophages. As shown in Fig. 8C, expression of CD86 (green) with plaques was significantly reduced after treated with MMON@PL,

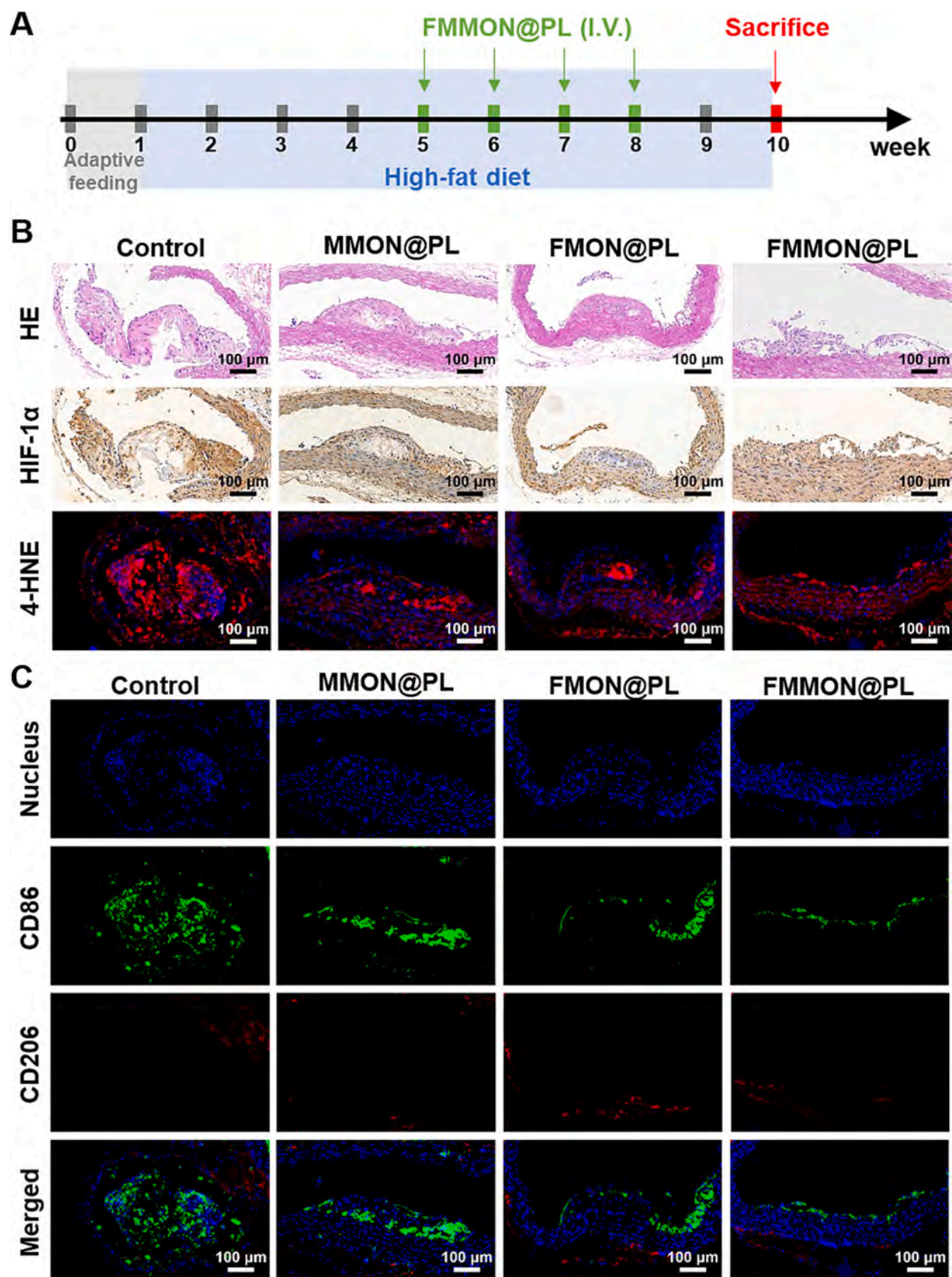


Fig. 8. Timeline diagram of the animal experiment. (B) Histopathological staining of plaques from mice treated with MMON@PL, FMON@PL and FMMON@PL. (C) Immunofluorescence images of double staining for CD86 and CD206 to label M1- or M2-type macrophages.

FMON@PL and FMMON@PL. Among them, FMMON@PL exhibited better inhibition of M1-type macrophages than MMON@PL and FMMON@PL. However, M2-type macrophages were barely observed in plaques in all groups. These results again suggested that oxygen supply significantly alleviated the plaque inflammatory microenvironment by suppressing the M1 phenotype rather than promoting the M2 phenotype.

Finally, biosafety is another aspect that needs to be examined. As shown in Fig. S20, it showed that the hemolysis rate was only 6.4 % even at a concentration of 0.2 mg/mL, indicating decent hemocompatibility of FMMON@PL. Given the presence of platelet membranes, coagulation tests were conducted. As shown in Fig. S21, FMMON@PL did not cause coagulation. Another concern is whether the presence of IONPs promote ferroptosis. GSH content and the typical ferroptosis indicators, glutathione peroxidase 4 (GPX4) and SLC7A11/xCT were evaluated. As shown in Fig. S22, GSH content decreased by 55.3 % and 45.8 % respectively by after IONPs and FMMON@P treatment. And the expression of GPX4 and xCT decreased by 62.3 % and 61.8 % respectively after IONPs and FMMON@P treatment. However, FMMON@PL hardly reduced GSH content and the expression of GPX4 and xCT. These results indicated that IONPs and FMMON@P promoted the ferroptosis. However, FMMON@PL barely affected ferroptosis, probably resulted from timely lysosomal escape of FMMON@PL.

After tail vein injection, the number of FMMON@PL in blood circulation decreased over time. As shown in Fig. S23, it decreased by 30.8 %, 59.7 % and 73.6 % after 12 h, 24 h and 48 h post injection, respectively. In addition, FMMON@PL accumulated mainly in livers and kidneys (Fig. S24), suggesting possible metabolism through liver and kidney. Slightly elevated FMMON@PL were also observed in liver and kidney by Prussian blue staining (Fig. S25), which is consistent with the results in Fig. S18. However, no tissue damage to organs can be observed by HE staining, especially in liver and kidney (Fig. S26). These results demonstrated the good biosafety of FMMON@PL.

4. Conclusion

In conclusion, FMMON@PL successfully achieved oxygen delivery within atherosclerotic plaques. FMMON@PL directly ameliorated plaque hypoxia, leading to reduced ROS levels and inhibiting HIF-1 α accumulation and nuclear translocation. FMMON@PL also enhanced cholesterol efflux and inhibited uptake of ox-LDL, leading to reduced foam cell formation. Not only that, FMMON@PL also inhibited macrophage differentiation to proinflammatory M1-type macrophages, improving the proinflammatory environment within the plaque. FMMON@PL successfully achieved oxygen delivery within plaques and inhibited plaque progression, demonstrating the feasibility of alleviating hypoxia for the treatment of atherosclerosis.

CRediT authorship contribution statement

Yujie Wang: Writing – original draft, Software, Methodology, Investigation, Formal analysis, Data curation. **Qianru Zhou:** Writing – review & editing, Visualization, Methodology, Formal analysis, Data curation. **Le Lu:** Methodology, Investigation. **Jianhua Xu:** Methodology, Investigation. **Gang Yang:** Methodology, Investigation. **Xuan Sun:** Methodology, Investigation. **Xue Bao:** Methodology, Data curation. **Lina Kang:** Methodology, Data curation. **Pin Lv:** Methodology. **Renyuan Liu:** Methodology. **Biao Xu:** Validation, Supervision. **Qi Yang:** Validation, Supervision. **Dan Mu:** Supervision, Resources, Project administration, Funding acquisition. **Bing Zhang:** Supervision, Project administration.

Declaration of competing interest

No data was used for the research described in the article.

Acknowledgments

This work was supported by the National Natural Science Foundation of China (82272065); Medical Research Project of Jiangsu Health Commission in 2022 (M2022066); the Nanjing Medical Science and technique Development Foundation (ZKX23019, ZKX19018); the 15th special supported project of China Postdoctoral Science Foundation (2022 T150317), and Nanjing Gulou Hospital New Technology Development Fund (XJSFZJJ202026, XJSFZLX202114).

Appendix A. Supplementary data

Supplementary data to this article can be found online at <https://doi.org/10.1016/j.jconrel.2025.02.053>.

Data availability

Data will be made available on request.

References

- [1] B. Pang, G. Dong, T. Pang, X. Sun, X. Liu, Y. Nie, X. Chang, Emerging insights into the pathogenesis and therapeutic strategies for vascular endothelial injury-associated diseases: focus on mitochondrial dysfunction, *Angiogenesis* (2024), <https://doi.org/10.1007/s10456-024-09938-4>.
- [2] J. Tarbell, M. Mahmoud, A. Corti, L. Cardoso, C. Caro, The role of oxygen transport in atherosclerosis and vascular disease, *J. R. Soc. Interface* 17 (2020) 20190732.
- [3] C. Stroebe, F.S. Nettersheim, B. Coon, A.C. Finney, M.A. Schwartz, K. Ley, O. Rom, A. Yurdagul, Dysregulated cellular metabolism in atherosclerosis: mediators and therapeutic opportunities, *Nat. Metab.* 6 (2024) 617–638.
- [4] M. Gao, M. Tang, W. Ho, Y. Teng, Q. Chen, L. Bu, X. Xu, X.Q. Zhang, Modulating plaque inflammation via targeted mRNA nanoparticles for the treatment of atherosclerosis, *ACS Nano* 17 (2023) 17721–17739.
- [5] X. Lu, Z. He, X. Xiao, X. Wei, X. Song, S. Zhang, Natural antioxidant-based Nanodrug for atherosclerosis treatment, *Small* 19 (2023) 1–10.
- [6] T. McGarry, M. Biniecka, D.J. Veale, U. Fearon, Hypoxia, oxidative stress and inflammation, *Free Radic. Biol. Med.* 125 (2018) 15–24.
- [7] P. Hou, J. Fang, Z. Liu, Y. Shi, M. Agostini, F. Bernassola, P. Bove, E. Candi, V. Rovella, G. Sica, Q. Sun, Y. Wang, M. Scimeca, M. Federici, A. Mauriello, G. Melino, Macrophage polarization and metabolism in atherosclerosis, *Cell Death Dis.* 14 (2023) 691.
- [8] T. Laval, M. Ouimet, A role for lipophagy in atherosclerosis, *Nat. Rev. Cardiol.* 20 (2023) 431–432.
- [9] G.R.Y. De Meyer, M. Zurek, P. Puylaert, W. Martinet, Programmed death of macrophages in atherosclerosis: mechanisms and therapeutic targets, *Nat. Rev. Cardiol.* 21 (2024) 312–325.
- [10] A. Aarup, T.X. Pedersen, N. Junker, C. Christoffersen, E.D. Bartels, M. Madsen, C.H. Nielsen, L.B. Nielsen, Hypoxia-inducible factor-1 α expression in macrophages promotes development of atherosclerosis, *Arterioscler. Thromb. Vasc. Biol.* 36 (2016) 1782–1790.
- [11] T. Jain, E.A. Nikolopoulou, Q. Xu, A. Qu, Hypoxia inducible factor as a therapeutic target for atherosclerosis, *Pharmacol. Ther.* 183 (2018) 22–33.
- [12] A.F. McGettrick, L.A.J. O'Neill, The role of HIF in immunity and inflammation, *Cell Metab.* 32 (2020) 524–536.
- [13] E. Karshovska, Y. Wei, P. Subramanian, R. Mohibullah, C. Geißler, I. Baatsch, A. Popal, J. Corbalán Campos, N. Exner, A. Schober, HIF-1 α (hypoxia-inducible factor-1 α) promotes macrophage necroptosis by regulating miR-210 and miR-383, *Arterioscler. Thromb. Vasc. Biol.* 40 (2020) 583–596.
- [14] N. Villa-Roel, K. Ryu, L. Gu, J. Fernandez Esmerats, D.W. Kang, S. Kumar, H. Jo, Hypoxia inducible factor 1 α inhibitor PX-478 reduces atherosclerosis in mice, *Atherosclerosis* 344 (2022) 20–30.
- [15] B. Qiu, P. Yuan, X. Du, H. Jin, J. Du, Y. Huang, Hypoxia inducible factor-1 α is an important regulator of macrophage biology, *Heliyon* 9 (2023) e17167.
- [16] F. Zhang, J. Zhuang, B. Esteban Fernández De Ávila, S. Tang, Q. Zhang, R.H. Fang, L. Zhang, J. Wang, A nanomotor-based active delivery system for intracellular oxygen transport, *ACS Nano* 13 (2019) 11996–12005.
- [17] C. Zhang, Q. Yan, J. Li, Y. Zhu, Y. Zhang, Nanoenabled tumor oxygenation strategies for overcoming hypoxia-associated immunosuppression, *ACS Appl. Bio Mater.* 4 (2021) 277–294.
- [18] X. Li, Y. Wu, R. Zhang, W. Bai, T. Ye, S. Wang, Oxygen-based Nanocarriers to modulate tumor hypoxia for ameliorated anti-tumor therapy: fabrications, properties, and future directions, *Front. Mol. Biosci.* 8 (2021) 1–25.
- [19] N. Kakaie, R. Amirian, M. Azadi, G. Mohammadi, Z. Izadi, Perfluorocarbons: a perspective of theranostic applications and challenges, *Front. Bioeng., Biotechnol.* 11 (2023) 1–16.
- [20] Q. Ye, D. Zheng, K. Chen, H. Xu, Z. Yang, J. Wen, Y. Hu, J. Wu, Phase-change based oxygen carriers improve acute cerebral hypoxia, *Small* 2309180 (2023) 1–11.
- [21] Y. Yang, Y. Liu, Y. Jiang, Recent advances in perfluorocarbon-based delivery Systems for Cancer Theranostics, *Mol. Pharm.* 20 (2023) 3254–3277.

- [22] J. Duan, S. Zhao, Y. Duan, D. Sun, G. Zhang, D. Yu, Y. Lou, H. Liu, S. Yang, X. Liang, C. Ma, H. Liu, J. Qiu, L. Gao, Y. Sang, Mnox Nanoenzyme armed CAR-NK cells enhance solid tumor immunotherapy by alleviating the immunosuppressive microenvironment, *Adv. Healthc. Mater.* 13 (2024) 1–13.
- [23] S. Wang, M. Cheng, S. Wang, W. Jiang, F. Yang, X. Shen, L. Zhang, X. Yan, B. Jiang, K. Fan, A self-catalytic NO/O₂ gas-releasing Nanozyme for radiotherapy sensitization through vascular normalization and hypoxia relief, *Adv. Mater.* 2403921 (2024) 1–20.
- [24] J. Zhang, W. Li, Z. Tao, X. Zhou, X. Chen, J. Zhou, H. Sun, Y. Fang, Y. Liu, Endogenous glucose-driven cascade reaction of nano-drug delivery for boosting multidrug-resistant bacteria-infected diabetic wound healing, *J. Colloid Interface Sci.* 672 (2024) 63–74.
- [25] R. Wang, J. Li, X. Wang, Y. Zhang, A. Zhu, K. Feng, J. Li, L. Di, Personalized Nanovaccines enhance lymph node accumulation and reprogram the tumor microenvironment for improved photodynamic immunotherapy, *Nano Lett.* 24 (2024) 7432–7442.
- [26] T. Haase, A. Ludwig, A. Stach, A. Mohtashamdolatsahi, R. Hauptmann, L. Mundhenk, H. Kratz, S. Metzkow, A. Kader, C. Freise, S. Mueller, N. Stolzenburg, P. Radon, M. Liebl, F. Wiekhorst, B. Hamm, M. Taupitz, J. Schnorr, Repeated injection of very small superparamagnetic Iron oxide particles (VSOPs) in murine atherosclerosis: a safety study, *Nanomaterials* 14 (2024) 773.
- [27] C. Huang, W. Huang, Y. Meng, C. Zhou, X. Wang, C. Zhang, Y. Tian, W. Wei, Y. Li, Q. Zhou, W. Chen, Y. Tang, T1-weighted MRI of targeting atherosclerotic plaque based on CD40 expression on engulfed USPIO's cell surface, *Biomed. Mater.* 19 (2024) 025019.
- [28] K.C. Briley-Saebo, Y.S. Cho, P.X. Shaw, S.K. Ryu, V. Mani, S. Dickson, E. Izadmehr, S. Green, Z.A. Fayad, S. Tsimikas, Targeted iron oxide particles for in vivo magnetic resonance detection of atherosclerotic lesions with antibodies directed to oxidation-specific epitopes, *J. Am. Coll. Cardiol.* 57 (2011) 337–347.
- [29] A. Ghazzy, H. Nsairat, R. Said, O.A. Sibai, A. AbuRuman, A.S. Shraim, A. Al Hunaiti, Magnetic iron oxide-based nanozymes: from synthesis to application, *Nanoscale Adv.* 6 (2024) 1611–1642.
- [30] Z. Yi, X. Yang, Y. Liang, S. Tong, Iron oxide nanozymes enhanced by ascorbic acid for macrophage-based cancer therapy, *Nanoscale* (2024) 14330–14338.
- [31] J. Yang, J. Zhu, B. Ren, H. Cai, Z. Li, Q. Fan, W. Xiong, J. Feng, C. Yan, G. Wen, Y. Li, C. Chen, Z. Shen, A hollow mesoporous iron oxide nanoparticle to strengthen Fenton reaction and weaken antioxidant defense systems for high efficacy tumor ferroptosis therapy, *Chem. Eng. J.* 497 (2024) 154470.
- [32] S. Sabnis, E.S. Kumarasinghe, T. Salerno, C. Mihai, T. Ketova, J.J. Senn, A. Lynn, A. Bulychev, I. McFadyen, J. Chan, Ö. Almarsson, M.G. Stanton, K.E. Benenato, A novel amino lipid series for mRNA delivery: improved endosomal escape and sustained pharmacology and safety in non-human Primates, *Mol. Ther.* 26 (2018) 1509–1519.
- [33] S.Y. Cheon, E.J. Kim, J.M. Kim, E.H. Kam, B.W. Ko, B.N. Koo, Regulation of microglia and macrophage polarization via apoptosis signal-regulating kinase 1 silencing after ischemic/hypoxic injury, *Front. Mol. Neurosci.* 10 (2017) 1–14.
- [34] L. Chen, Y. Gao, Y. Li, C. Wang, D. Chen, Y. Gao, X. Ran, Severe intermittent hypoxia modulates the macrophage phenotype and impairs wound healing through downregulation of HIF-2 α , *Nat. Sci. Sleep.* 14 (2022) 1511–1520.
- [35] S.C. Pias, How does oxygen diffuse from capillaries to tissue mitochondria? Barriers and pathways, *J. Physiol.* 599 (2021) 1769–1782.
- [36] C. Lops, A. Ancona, K. Di Cesare, B. Dumontel, N. Garino, G. Canavese, S. Hernández, V. Cauda, Sonophotocatalytic degradation mechanisms of rhodamine B dye via radicals generation by micro- and nano-particles of ZnO, *Appl. Catal. B Environ.* 243 (2019) 629–640.
- [37] M. Crucet, S.J.A. Wüst, P. Spielmann, T.F. Lüscher, R.H. Wenger, C.M. Matter, Hypoxia enhances lipid uptake in macrophages: role of the scavenger receptors Lox1, SRA, and CD36, *Atherosclerosis* 229 (2013) 110–117.
- [38] Y. Chen, H. Wang, J. Pan, Y. Guo, Y. Hu, X. Huang, Y. Zhou, Q. Deng, Q. Zhou, Macrophage-targeted ultrasound nanobubbles for highly efficient sonodynamic therapy of atherosclerotic plaques by modulating M1-to-M2 polarization, *Atherosclerosis* 389 (2024) 117423.